PNAS RESEARCH ARTICLE | BIOCHEMISTRY

Selective involvement of UGGT variant: UGGT2 in protecting mouse embryonic fibroblasts from saturated lipid-induced ER stress

Hui-Hsing Hung[a], Yasuko Nagatsuka[a], Tatiana Soldà[b], Vamsi K. Kodali[c], Kazuhisa Iwabuchi[d], Hiroyuki Kamiguchi[a], Koki Kano[e], Ichiro Matsuo[e], Kazutaka Ikeda[f], Randal J. Kaufman[c], Maurizio Molinari[b,g], Peter Greimel[a], and Yoshio Hirabayashi[d,h,1]

Edited by Randy Schekman, University of California, Berkeley, Department of Molecular and Cell Biology, Berkeley, CA; received September 8, 2022; accepted October 25, 2022

Secretory proteins and lipids are biosynthesized in the endoplasmic reticulum (ER). The "protein quality control" system (PQC) monitors glycoprotein folding and supports the elimination of terminally misfolded polypeptides. A key component of the PQC system is Uridine diphosphate glucose:glycoprotein glucosyltransferase 1 (UGGT1). UGGT1 re-glucosylates unfolded glycoproteins, to enable the re-entry in the protein-folding cycle and impede the aggregation of misfolded glycoproteins. In contrast, a complementary "lipid quality control" (LQC) system that maintains lipid homeostasis remains elusive. Here, we demonstrate that cytotoxic phosphatidic acid derivatives with saturated fatty acyl chains are one of the physiological substrates of UGGT2, an isoform of UGGT1. UGGT2 produces lipid raft-resident phosphatidylglucoside regulating autophagy. Under the disruption of lipid metabolism and hypoxic conditions, UGGT2 inhibits PERK-ATF4-CHOP-mediated apoptosis in mouse embryonic fibroblasts. Moreover, the susceptibility of UGGT2 KO mice to high-fat diet-induced obesity is elevated. We propose that UGGT2 is an ER-localized LQC component that mitigates saturated lipid-associated ER stress via lipid glucosylation.

UGGT | hypoxia | saturated lipid | phosphatidylglucoside | CHOP

Significance

Our manuscript demonstrates that UGGT2-mediated lipid glucosylation, analogous to the well-established UGGT1-mediated unfolded protein glucosylation, is an essential component of the endoplasmic reticulum quality control (ERQC) system, specifically under hypoxic conditions. Prior research commonly associates UGGT2 with the protein–ERQC system, primarily based on the homology of its catalytic subunit with UGGT1. This report shows that UGGT2 mediates lipid glucosylation to mitigate ER stress. Our findings are not limited to basic lipid biochemistry but provide a fresh perspective on lipid-induced ER stress.

A substantial proportion of the total protein and lipid biosynthesis in cells occurs within the endoplasmic reticulum (ER) network (1, 2). The failure of the ER to handle the required synthetic load (ER stress) plays a key role in the pathogenesis of many diseases, such as diabetes, Alzheimer's and Parkinson's disease, and cancer (3). ER homeostasis is maintained by sophisticated machinery responsible for correct protein folding and lipid metabolism. The disruption of protein-folding homeostasis accompanied by an increase in misfolded proteins is detected by a set of ER transmembrane sensors, such as inositol-requiring enzyme 1 (IRE1) and pancreatic endoplasmic reticulum kinase (PERK). These sensors activate the unfolded protein response (UPR) signaling pathway (4). Uridine diphosphate (UDP)-glucose:glycoprotein glucosyltransferase 1 (UGGT1), a key component of the protein quality control (PQC) system, glucosylates unfolded/misfolded proteins to facilitate their re-entry into the protein-folding cycle and in turn reduce the accumulation of misfolded proteins in the ER (5, 6).

High levels of saturated fatty acids (sFAs) also induce ER stress, similarly activating the UPR signaling pathway. Both IRE1 and PERK directly sense the quality and saturation of lipids in the ER via their transmembrane domains (7–10). This suggests that the UPR signaling pathway evolved to simultaneously and cooperatively resolve ER stress caused by disturbances in the quality of proteins and lipids. However, an equivalent lipid quality control (LQC) system remains elusive. It seems plausible that such an LQC analog of the well-established PQC system should also be capable of preventing ER stress.

The importance of UGGT1 in PQC and its role in mitigating ER stress is widely accepted. The biological function of UGGT1's paralogue, UDP-glucose:glycoprotein glucosyltransferase 2 (UGGT2), remains less well defined (11, 12), even though it has been recently proposed to play an important role in the maturation of some lysosomal proteins (13). A variety of clinical studies have reported changes in UGGT2 expression, such as elevated UGGT2 levels in the prefrontal cortex of schizophrenia patients (14, 15). In addition, *UGGT2* gene expression in pancreatic β-cells derived from patients diagnosed with type II diabetes is significantly reduced compared to β-cells derived from age-matched healthy controls (16). Both disorders are associated with the dysregulation of lipid homeostasis, more specifically an imbalance in lipid saturation.

Here, we demonstrate that UGGT2 is largely unnecessary for efficient protein biogenesis, but essential for regulating lipid metabolism. The loss of UGGT2 in mice increased

Author contributions: H.-H.H., Y.N., K.Iwabuchi., H.K., M.M., P.G., and Y.H. designed research; H.-H.H., Y.N., T.S., V.K.K., K.Ikeda., R.J.K., M.M., and P.G. performed research; K.K., I.M., and P.G. contributed new reagents/analytic tools; H.-H.H. analyzed data; K.Iwabuchi., H.K., I.M., R.J.K., M.M., and Y.H. supervised research; and H.-H.H., I.M., K.Ikeda., R.J.K., M.M., P.G., and Y.H. wrote the paper.

The authors declare no competing interest.

This article is a PNAS Direct Submission.

[1]To whom correspondence may be addressed. Email: hirabaya@riken.jp.

This article contains supporting information online at https://www.pnas.org/lookup/suppl/doi:10.1073/pnas.2214957119/-/DCSupplemental.

Published December 12, 2022.

susceptibility to high-fat diet (HFD)-induced obesity. We identified the saturated phosphatidic acid (sPA with C18:0/C20:0) as one of the suitable acceptors for UGGT2-driven glucosylation, yielding phosphatidyl-β-D-glucoside (PtdGlc). UGGT2 but not UGGT1 was protective during hypoxic stress by positively modulating autophagy and mitigating PERK-C/EBP homologous Protein (CHOP)-mediated apoptosis. Together, our results demonstrate that UGGT2-dependent lipid glucosylation ensures the sufficient quality of lipids and mitigates ER stress.

Results

***Uggt2* Deletion Does Not Impair Protein Folding but Increases HFD-Induced Obesity.** *Uggt1* and *Uggt2* share a high sequence identity in their C-terminal catalytic domain (17), but differ markedly in the very large N-terminal region responsible for substrate recognition. In vitro, both isoforms have glucosyl transferase activity toward synthetic substrates that mimic immature proteins, albeit UGGT2 exhibited only a very low activity (18).

We found that in the presence of UGGT1, UGGT2 is not essential for efficient protein biogenesis, even under elevated biosynthetic load (*SI Appendix*, Fig. S1). The result prompted us to investigate the role of UGGT2 in the regulation of lipid homeostasis. sFAs that arise from de novo biosynthesis, recycling pathway, or nutrient uptake are efficiently converted to unsaturated fatty acids (uFAs) by ER-associated stearoyl-CoA desaturase (SCD) (19). The knockdown of *Scd* in vivo has been reported to induce ER stress (9). The treatment of Wild-type (WT), UGGT1 knockout (KO), and UGGT2 KO mouse embryonic fibroblasts (MEFs) with CAY10566 (5 μM, for 24 h), a known inhibitor of SCD1, disrupted ER lipid homeostasis, and the activation of the UPR signaling pathway was assessed by western blot (Fig. 1 *A*–*H*). The expression of phosphorylated PERK was significantly increased only in UGGT2 KO MEFs (Fig. 1*B*). Correspondingly, the expression of ATF4, a downstream transcription factor of PERK, and the proapoptotic transcription factor CHOP was significantly higher in UGGT2 KO MEFs compared to WT and UGGT1 KO MEFs (Fig. 1 *C* and *D*). The expression of two other ER stress sensors, namely phosphorylated IRE1α and cleaved ATF6, was not altered (Fig. 1 *E*–*H*). This suggests that in the absence of UGGT2, SCD inhibitor-induced disruption of lipid homeostasis could not be restored, fuelling activation of the PERK-CHOP-regulated apoptotic pathway.

In contrast, the disruption of protein homeostasis by tunicamycin-induced (1 μM, for 24 h) accumulation of misfolded proteins activated the PERK-ATF4-CHOP signaling pathway in WT, UGGT1 KO, and UGGT2 KO MEFs (Fig. 1 *I*–*L*). Concurrently, the expression of phosphorylated IRE1α and cleaved ATF6 was not altered (Fig. 1 *M*–*P*). Taken together, these results imply the involvement of UGGT2 in mitigating ER stress associated with the dysregulation of lipid homeostasis but not protein homeostasis.

Uggt1 deletion but not *Uggt2* deletion in mice has been reported to be embryonically lethal (20). To date, no obvious phenotype has been identified in UGGT2 KO mice. We found that loss of *Uggt2* in mice increased susceptibility to HFD-induced obesity (*SI Appendix*, Fig. S2). In addition, HFD-fed UGGT2 KO mice exhibited significantly elevated fasting glucose levels compared to the regular-fat diet-fed control group. These findings indicate that UGGT2 plays an important role in maintaining lipid homeostasis under high-fat-diet-induced stress conditions. Considering the previously reported glucosyl transferase activity of UGGT2 (18), we hypothesized that UGGT2 might catalyze the glucosylation of lipid substrates.

UGGT2-Catalyzed Glucosylation of sPA Yields PtdGlc In Vitro. In mammals, only three glucosylated lipids have been identified to date, namely glucosylceramide (GlcCer), cholesteryl glucoside (GlcChol), and phosphatidylglucoside (PtdGlc) (21). GlcCer is biosynthesized in the Golgi apparatus by UDP-glucose ceramide glucosyltransferase (22), while GlcChol is biosynthesized by glucocerebrosidase (23). To date, the enzymes involved in the biosynthesis of PtdGlc and the origin of its fairly unusual fully saturated acyl chain pattern remain elusive (24). Contemplating the potential involvement of UGGT2 in the biosynthesis of PtdGlc would require glucosylation of a suitable phosphatidic acid (PA) acceptor.

First, we established an in vitro PtdGlc biosynthesis assay to investigate the suitability of PA derivatives as UGGT2 substrates. PtdGlc formation was monitored by reversed-phase LC-MS/MS in negative ion mode with multiple reaction monitoring. Synthetic PtdGlc (18:0/20:0) standard exhibited qualifier ion transitions with a mass-to-charge ratio (*m/z*) of $[M–H]^-$ 893.5 → 419.1 for loss of glucosyl and arachidoyl (20:0) moieties, $[M–H]^-$ 893.5 → 311.2 of the arachidoyl (20:0) fragment, $[M–H]^-$ 893.5 → 283.1 of the stearoyl (18:0) fragment, and $[M–H]^-$ 893.5 → 79.0 of the phosphate fragment (Fig. 2*A*). Simultaneous monitoring of all qualifier ion transitions revealed a single elution time of 30.7 min in case of the synthetic PtdGlc standard (Fig. 2*B*).

The concentration and purity of all flag-conjugated UGGT preparations were monitored by Coomassie brilliant blue (CBB) staining (*SI Appendix*, Fig. S3), and each assay was performed with an identical amount of UGGT proteins. To mimic the native PtdGlc (18:0/20:0) acyl pattern, synthetic sPA featuring stearoyl (18:0) and arachidoyl (20:0) moieties was employed as a glucosyl acceptor, while UDP-glucose acted as donor substrate. The incubation with buffer or purified flag-conjugated UGGT1 exhibited no statistically significant difference. By contrast, the incubation with purified flag-conjugated UGGT2 produced a clear PtdGlc-positive signal at 30.7 min (Fig. 2 *C* and *D*). The fragmentation pattern and relative ion yield of the synthetic PtdGlc standard (Fig. 2*E*) and PtdGlc derived from the UGGT2-catalyzed reaction were identical (Fig. 2*F*). However, the incubation of unsaturated PA (uPA, 18:1/18:1) with flag-conjugated UGGT2 did not produce any glucosylated-uPA-positive signal (Fig. 2*G*). These results suggest that UGGT2 is capable to catalyze the transfer of the glucose residue from UDP-glucose to the saturated lipid acceptor, sPA (18:0/20:0), yielding PtdGlc.

PtdGlc Levels Are Reduced in UGGT1- and UGGT2-Deficient MEFs. To investigate the relationship of PtdGlc and UGGT2 in a cellular environment, PtdGlc levels in WT, UGGT1 KO, and UGGT2 KO MEFs were analyzed (Fig. 3 *A*–*C*). Normalized PtdGlc levels in UGGT2 KO MEFs were significantly reduced compared to WT MEFs. This is in line with our in vitro biosynthesis assay results further corroborating the involvement of UGGT2 in the biosynthesis of PtdGlc.

However, the significant reduction in PtdGlc levels observed in UGGT1 KO MEFs was not readily apparent, especially considering the increased total UGGT2 protein levels detected by western blot upon *Uggt1* deletion (Fig. 3 *D* and *E*). This genetic compensation could arise due to increased interaction of the large hydrophobic N-terminal domain of UGGT2 with unfolded/misfolded proteins in the absence of UGGT1 and seems consistent with the previously reported glucosyltransferase activity towards synthetic immature protein-mimetic substrates (18). Previously, urea-denatured thyroglobulin (Tg) was identified as a reactive UGGT1 substrate (25). To determine whether unfolded/misfolded proteins do indeed compete with sPA for UGGT2, we performed

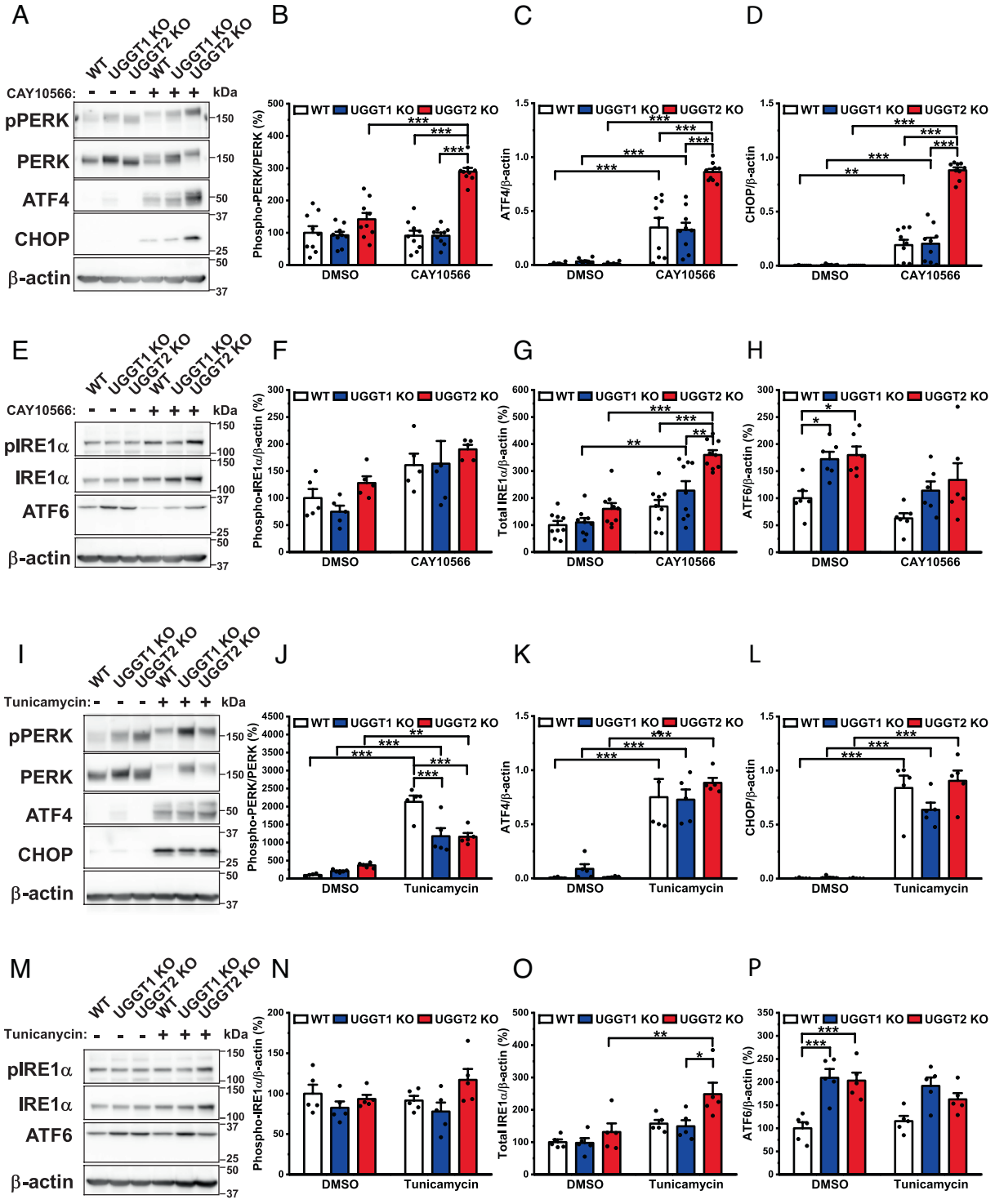

Fig. 1. *Uggt2* deletion only enhances saturated lipid-induced ER stress. (*A*) Representative western blots of phospho-PERK, PERK, ATF4, and CHOP from MEFs treated with CAY10566 (5 μM, for 24 h). (*B*) Average normalized phospho-PERK levels ($N = 9$). (*C*) Average normalized ATF4 levels ($N = 9$). (*D*) Average normalized CHOP levels ($N = 9$). (*E*) Representative western blots of phospho-IRE1α, IRE1α, and cleaved ATF6 from MEFs treated with CAY10566 (5 μM, for 24 h). (*F*) Average normalized phospho-IRE1α levels ($N = 5$). (*G*) Average normalized IRE1α levels ($N = 9$). (*H*) Average normalized cleaved ATF6 levels ($N = 6$). (*I*) Representative western blots of phospho-PERK, PERK, ATF4, and CHOP from MEFs treated with tunicamycin (1 μM, for 24 h). (*J*) Average normalized phospho-PERK levels ($N = 5$). (*K*) Average normalized ATF4 levels ($N = 5$). (*L*) Average normalized CHOP levels ($N = 5$). (*M*) Representative western blots of phospho-IRE1α, IRE1α, and cleaved ATF6 from MEFs treated with tunicamycin (1 μM, for 24 h). (*N*) Average normalized phospho-IRE1α levels ($N = 5$). (*O*) Average normalized IRE1α levels ($N = 5$). (*P*) Average normalized cleaved ATF6 levels ($N = 5$). Data are means ± SEM and were analyzed by two-way ANOVA followed by Tukey's multiple comparison post hoc test; $^{*}P < 0.05$, $^{**}P < 0.01$, $^{***}P < 0.001$.

PtdGlc biosynthesis assays with flag-conjugated UGGT2 in the presence of denatured Tg and sPA (18:0/20:0). Denatured Tg significantly inhibited UGGT2-dependent PtdGlc synthesis in vitro (Fig. 3*F*). In WT MEFs, tunicamycin-induced (10 μM, for 6 h) misfolded protein accumulation also resulted in reduced PtdGlc levels (Fig. 3*G*). Taken together, these results highlight the competition of sPA and unfolded/misfolded proteins for UGGT2 and rationalize the reduced PtdGlc levels in UGGT1 KO MEFs.

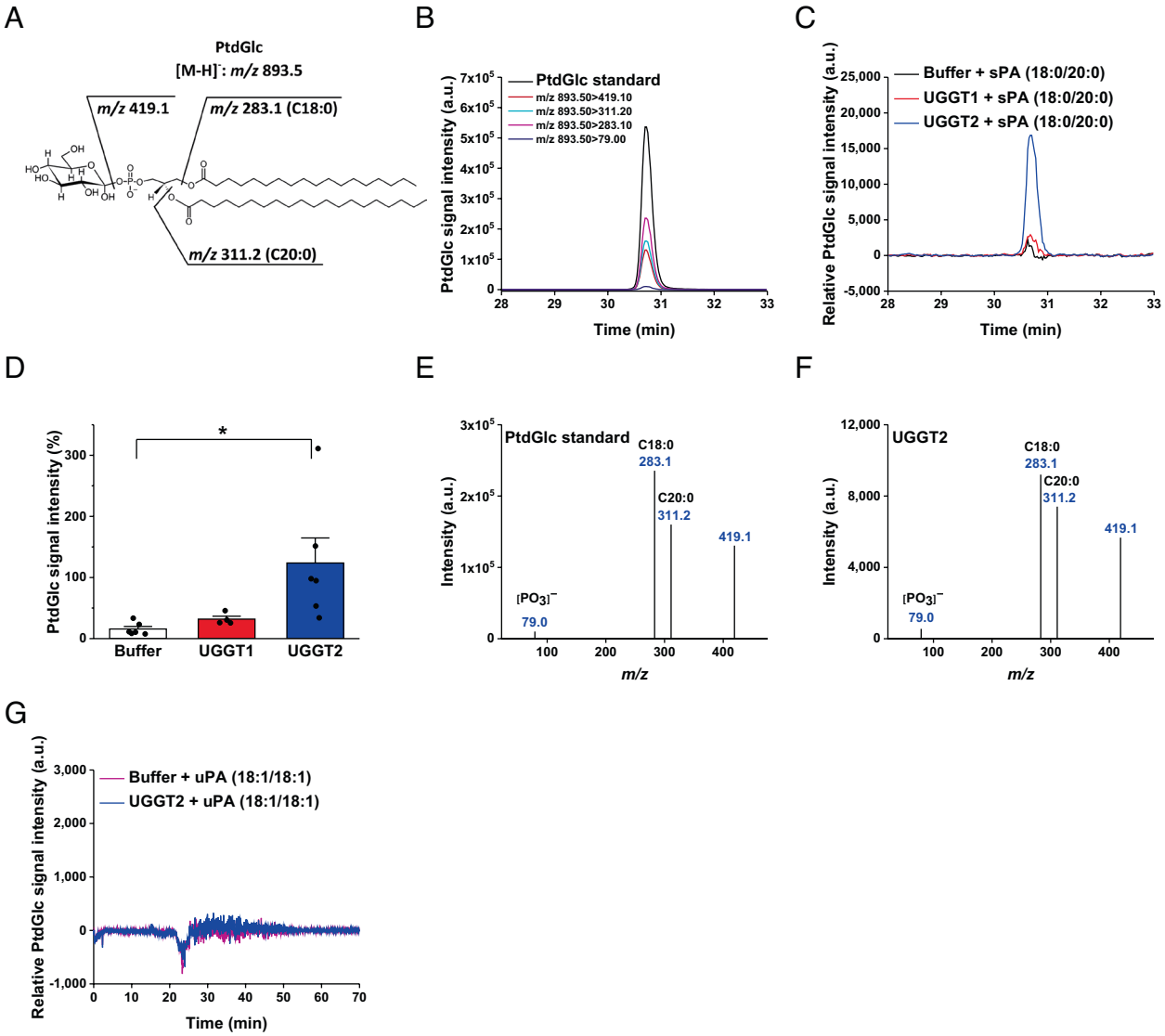

Fig. 2. UGGT2-catalyzed glucosylation of sPA yields PtdGlc in vitro. (*A*) Chemical structure of PtdGlc. The deprotonated molecular mass $[M–H]^-$ of PtdGlc is 893.5. (*B*) Representative trace of elution time of synthetic PtdGlc standard analyzed by LC-MS/MS; elution time is 30.7 min. (*C*) Representative traces of relative PtdGlc signals from buffer-sPA, UGGT1-sPA, or UGGT2-sPA incubation group. Data are displayed as the original signal minus the signal of the nonreaction control group. (*D*) Average normalized PtdGlc signal from buffer-sPA, UGGT1-sPA, or UGGT2-sPA incubation groups. Data are means ± SEM, with group differences evaluated by one-way ANOVA and Tukey's multiple comparison post hoc test ($N = 6$ for buffer-sPA and UGGT2-sPA incubation groups; $N = 4$ for UGGT1-sPA incubation group; $^*P < 0.05$). (*E*) Four peaks produced by the deprotonated PtdGlc at 30.7 min in (*B*): *m/z* 79.0 (PO_3^-), *m/z* 283.1 ($C_{18}H_{35}O_2^-$), *m/z* 311.2 ($C_{20}H_{39}O_2^-$), and *m/z* 419.1 ($C_{21}H_{40}O_6P^-$). (*F*) Four peaks produced by the deprotonated PtdGlc synthesized by UGGT2-catalyzed reaction in (*C*). (*G*) Representative traces of glucosylated-uPA (18:1/18:1) signals from buffer-uPA or UGGT2-uPA incubation group. Data are displayed as original signal minus the signal of the nonreaction control group.

The direct involvement of PERK in the biosynthesis of sPAs (26), the precursor of PtdGlc, raises the possibility that UGGT2-driven PtdGlc biosynthesis could be involved in reducing ER stress. Sustained ER stress inducer treatment has been suggested to promote lipid bilayer stress (27), as excessive accumulation of misfolded membrane proteins in the ER may lead to an abnormal protein-to-lipid ratio and local stretching of the lipid bilayer (28). Lipid bilayer stress such as increased lipid saturation in the ER membrane is directly detected by the transmembrane domains of IRE1 and PERK (10). Conversely, the inhibition of sPA formation prevents lipid bilayer stress-induced apoptosis (9). These results raise the possibility that UGGT2-driven PtdGlc biosynthesis could affect lipid bilayer stress tolerance. The reducing agent dithiothreitol (DTT) interferes with the formation of disulfide bridges in the lumen of the ER, resulting in ER stress (29). While short-term DTT treatment directly affects protein folding, extended DTT treatment (>4 h) induces lipid bilayer stress (27, 30).

To test the idea that UGGT2-driven PtdGlc biosynthesis could be involved in decreasing ER stress, we treated WT, UGGT1 KO, and UGGT2 KO MEFs with DTT (10 mM) for 6 h (Fig. 3*H*). PtdGlc levels were significantly increased in WT and UGGT1 KO MEFs, while PtdGlc levels in UGGT2 KO MEFs were unaffected. Next, we evaluated the effect of DTT on cell survival by MTT assay. Only the loss of UGGT2 but not UGGT1 significantly reduced the survival rate of MEFs compared to WT MEFs (Fig. 3*I*). These results indicate that PtdGlc biosynthesis correlates positively with lipid bilayer stress tolerance.

Effects of UGGT2-Dependent PtdGlc Synthesis on Autophagy under Hypoxic Conditions. Tumor tissue is known to develop hypoxic microenvironment that affects fatty acid biosynthesis (31). This is exemplified by reduced de novo biosynthesis of uFAs in solid tumors as the low oxygen levels suppress oxygen-requiring enzymes such as SCD (32). At the same time, de

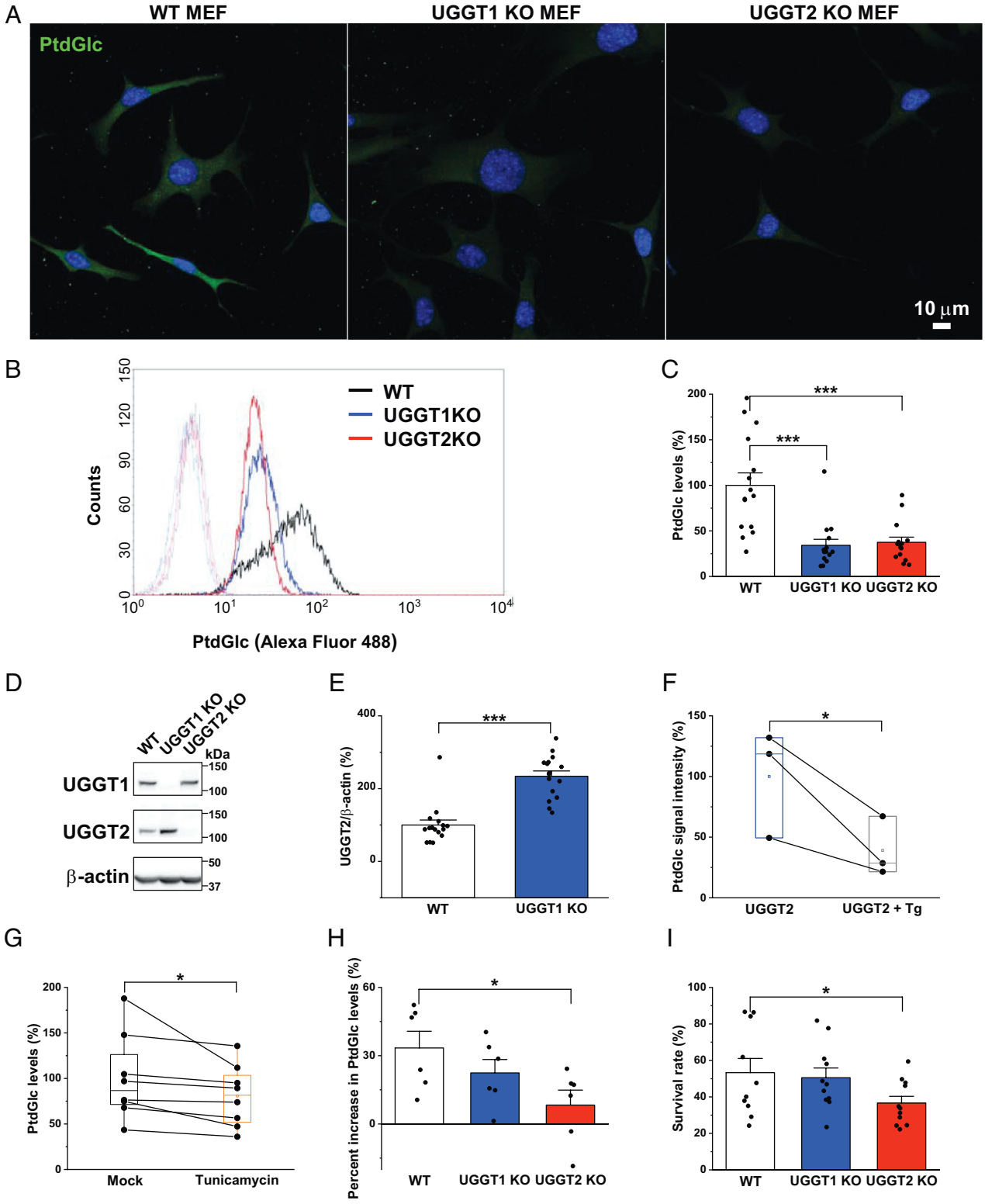

Fig. 3. PtdGlc levels are reduced in UGGT1- and UGGT2-deficient MEFs. (*A*) Representative confocal fluorescence images showing PtdGlc immunostaining (green) in WT, UGGT1 KO, and UGGT2 KO MEFs. Cells were counterstained with the nuclear stain DAPI (blue). (*B*) Representative flow cytometry histograms showing the levels of PtdGlc in WT, UGGT1 KO, and UGGT2 KO MEFs. (*C*) Average normalized PtdGlc levels in WT, UGGT1 KO, and UGGT2 KO MEFs. Statistical differences were assessed by one-way ANOVA followed by Tukey's multiple comparison post hoc test ($N = 15$). (*D*) Representative western blots of UGGT1 and UGGT2 from MEFs. (*E*) Average normalized UGGT2 levels. Data were analyzed by Student's t test ($N = 16$). (*F*) Normalized PtdGlc signal from UGGT2-sPA or UGGT2-sPA-Tg incubation groups. Data were analyzed by paired t test ($N = 3$); $^*P < 0.05$. (*G*) Normalized PtdGlc levels in WT MEFs treated with tunicamycin (10 μM, for 6 h). Statistical differences were assessed by Paired *t* test ($N = 8$); $^*P < 0.05$. (*H*) Average percent increase in PtdGlc levels in MEFs treated with DTT (10 mM, for 6 h). Data were analyzed by one-way ANOVA followed by Dunnett's multiple comparison post hoc test ($N = 9$). (*I*) Average normalized cellular survival rate of MEFs treated with DTT. Cellular survival was assessed with the MTT assay. Data were analyzed by one-way ANOVA followed by Dunnett's multiple comparison post hoc test ($N = 10$ for WT MEFs; $N = 11$ for UGGT1 KO and UGGT2 KO MEFs). Data are means ± SEM in (*C*), (*E*), (*H*), and (*I*); $^*P < 0.05$, $^{***}P < 0.001$.

novo sFA biosynthesis in hypoxic tumors is increased due to the upregulation of fatty acid synthase (33). The supplementation with exogenous uFA reduced IRE1-dependent apoptosis under tumor-like stress (32). Taking the above-outlined role of UGGT2 in restoring lipid homeostasis in the presence of SCD inhibitor into consideration, we contemplated the potential role of UGGT2 in alleviating hypoxia-associated lipid bilayer stress.

To this end, WT, UGGT1 KO, and UGGT2 KO MEFs were subjected to chemically induced hypoxic conditions by $CoCl_2$ treatment (200 μM, for 24 h). Western blot analysis confirmed the successful induction of hypoxic conditions by increased expression of hypoxia-inducible factor-1 alpha (HIF-1α) in all three cases (*SI Appendix*, Fig. S4 *A* and *B*). Concomitantly, the induction of chemical hypoxia was accompanied by a significant increase in cellular PtdGlc levels in WT MEFs (*SI Appendix*, Fig. S4*C*).

Immunofluorescence imaging of PtdGlc under chemically induced hypoxic conditions revealed punctate staining in WT and UGGT1 KO MEFs but not in UGGT2 KO MEFs (Fig. 4*A* and *SI Appendix*, Fig. S5*A*). Co-immunostaining with organelle markers lysosome-associated membrane protein 1 (LAMP1) and microtubule-associated protein 1A/1B-light chain 3 (LC3) localized the PtdGlc puncta to the autophagosomal and late endosomal/lysosomal (LE/Lys) compartment (Fig. 4 *B*, *C*, and *G* and *SI Appendix*, Fig. S5*B*). To further investigate the potential role of PtdGlc in autophagy and its associated transport pathway, WT MEFs were treated with bafilomycin A1 (BafA1). BafA1 is a known inhibitor of lysosomal maturation that consecutively inhibits autophagosome–lysosome fusion and degradation. Three main pathways that can deliver PtdGlc from the ER to autophagosomes and lysosomes are macro-ER-phagy, micro-ER-phagy, and ER-to-lysosome-associated degradation (ERLAD) (34). In macro-ER-phagy, ER fragments are enclosed by autophagosomes and subsequently fused with lysosomes. In micro-ER-phagy, a selected ER subdomain containing lipidated LC3 is directly engulfed by LE/Lys membranes (35), whereas in ERLAD, ER-derived vesicles directly fuse with lysosomes (36). The treatment with BafA1 (50 nM, for 25 h) induced the formation of ring-shaped PtdGlc aggregates (Fig. 4*D* and *SI Appendix*, Fig. S5*C*). These PtdGlc aggregates colocalized with LAMP1-positive vesicles (lysosomes) (Fig. 4*E*), while LC3-positive vesicles (autophagosomes) were observed inside PtdGlc-positive ring-shaped aggregates (Fig. 4*F*). In stress-free MEFs, no obvious PtdGlc puncta were observed (*SI Appendix*, Fig. S5*A*). Taken together, these results indicate that under basal conditions, synthesized PtdGlc is transported to lysosomes for degradation independently of the ER-phagy pathways. Under hypoxic conditions, PtdGlc seems to be involved in autophagosome–lysosome fusion because PtdGlc was localized to the LC3-positive vesicles instead of being degraded by lysosomes. It is tempting to speculate that the PtdGlc-LC3 positive vesicles are autolysosomes.

LC3 lipidation (LC3-I to LC3-II) is a key autophagy initiation step (37). Hence, LC3-II is a widely used marker for autophagosomes. Consistent with our immunofluorescence imaging results, autophagosome formation (LC3-II to β-actin ratio) was significantly elevated in WT MEFs under chemically induced hypoxic conditions (Fig. 4 *H* and *I*), while UGGT2 KO MEFs exhibited only a modest increase in autophagosome formation compared to WT MEFs. BafA1 treatment to impede LC3-II degradation confirmed that the reduced LC3-II levels in UGGT2 KO MEFs were caused by reduced LC3 lipidation but not increased degradation (Fig. 4 *H* and *J*). Taken together, this suggests that UGGT2-dependent PtdGlc formation plays an important role in autophagy under hypoxic conditions.

Chemical Hypoxia-Induced Lipid Bilayer Stress Activates PERK–CHOP-Regulated Apoptotic Pathway in UGGT2-Deficient Cells. Next, we examined the effect of $CoCl_2$ (200 μM, for 24 h) treatment in WT, UGGT1 KO, and UGGT2 KO MEFs on PA saturation. Chemical hypoxia increased PA saturation in all MEFs (Fig. 5 *A*–*C*) with the highest log2 fold increase in sPA (16:0/18:0) in UGGT2 KO MEFs compared to WT and UGGT1 KO MEFs (Fig. 5*B*).

sPAs but not uPAs induce ER stress and activate the UPR signaling pathway in human vascular smooth muscle cells (9). Therefore, we examined the effect of chemical hypoxia on the UPR signaling pathway in WT, UGGT1 KO, and UGGT2 KO MEFs by western blot. The expression of the ER stress sensors, phosphorylated IRE1α, and ATF6 was not altered (Fig. 5 *D*–*G*). In agreement with previous results (Fig. 1 *A*–*D*), the third UPR signaling pathway that comprised PERK-ATF4 was only activated in UGGT2 KO MEFs (Fig. 5 *H*–*J*). Correspondingly, the proapoptotic transcription factor CHOP was significantly increased only in UGGT2 KO cells (Fig. 5*K*). This indicates that in the absence of UGGT2, cells fail to maintain ER lipid homeostasis under sustained hypoxic conditions, leading to lipid bilayer stress and apoptosis.

To confirm the activation of the apoptotic pathway in UGGT2 KO MEFs under hypoxic conditions, we assessed the number of apoptotic cells by Annexin V-PI assay. Indeed, UGGT2 KO MEFs exhibited higher susceptibility to hypoxia-induced apoptosis (Fig. 5 *L* and *M*). Taken together, these results suggest that UGGT2 increases cell viability and reduces apoptotic cell death under lipid bilayer stress and highlights the importance of UGGT2 in regulating lipid homeostasis under stress conditions.

Discussion

In contrast to UGGT1, UGGT2 plays at most only a small role in the PQC system of the ER when UGGT1 exists. Our results reveal that UGGT2 is an indispensable component of the LQC system, a key enzyme in PtdGlc biosynthesis, and plays a key role in maintaining lipid homeostasis during hypoxia-induced lipid bilayer stress in the ER by positively modulating autophagy.

The *Uggt* gene is highly conserved across eukaryotes, but only in vertebrates and *Caenorhabditis* an independent gene duplication event occurred (11, 12). In both cases, the duplicated genes retained the glucosyl transferase function of the C-terminal catalytic domain, while the N-terminal recognition domain was subjected to extensive alterations. Hence, a distinct substrate preference for UGGT1 and UGGT2 seems credible. UGGT1 has been predicted to be localized in the ER lumen (38). However, UGGT2 was suggested not only to be localized in the ER lumen but also to associate with ER membrane even though no membrane-binding motif has been reported (38). This association with the ER membrane renders the interaction of UGGT2 with lipid substrates conceivable.

In *Caenorhabditis*, the current consensus suggests that the paralogous *uggt* genes have a divergent, nonredundant, ER stress-related function. Given the strong purifying selective pressure on the vertebrate *Uggt* gene, it has been proposed that *Uggt2* also has to benefit the survival of the host organism (11). While UGGT1 preferentially recognizes and glucosylates misfolded proteins, our in vitro results demonstrate that UGGT2 recognizes and glucosylates sPA, a lipid. Considering the reduced viability of UGGT2 KO MEFs under DTT-induced lipid bilayer stress, an increasingly similar picture in invertebrates compared to *Caenorhabditis* arises, suggesting a divergent, nonredundant, ER stress-related function of the vertebrate UGGT paralogues (11).

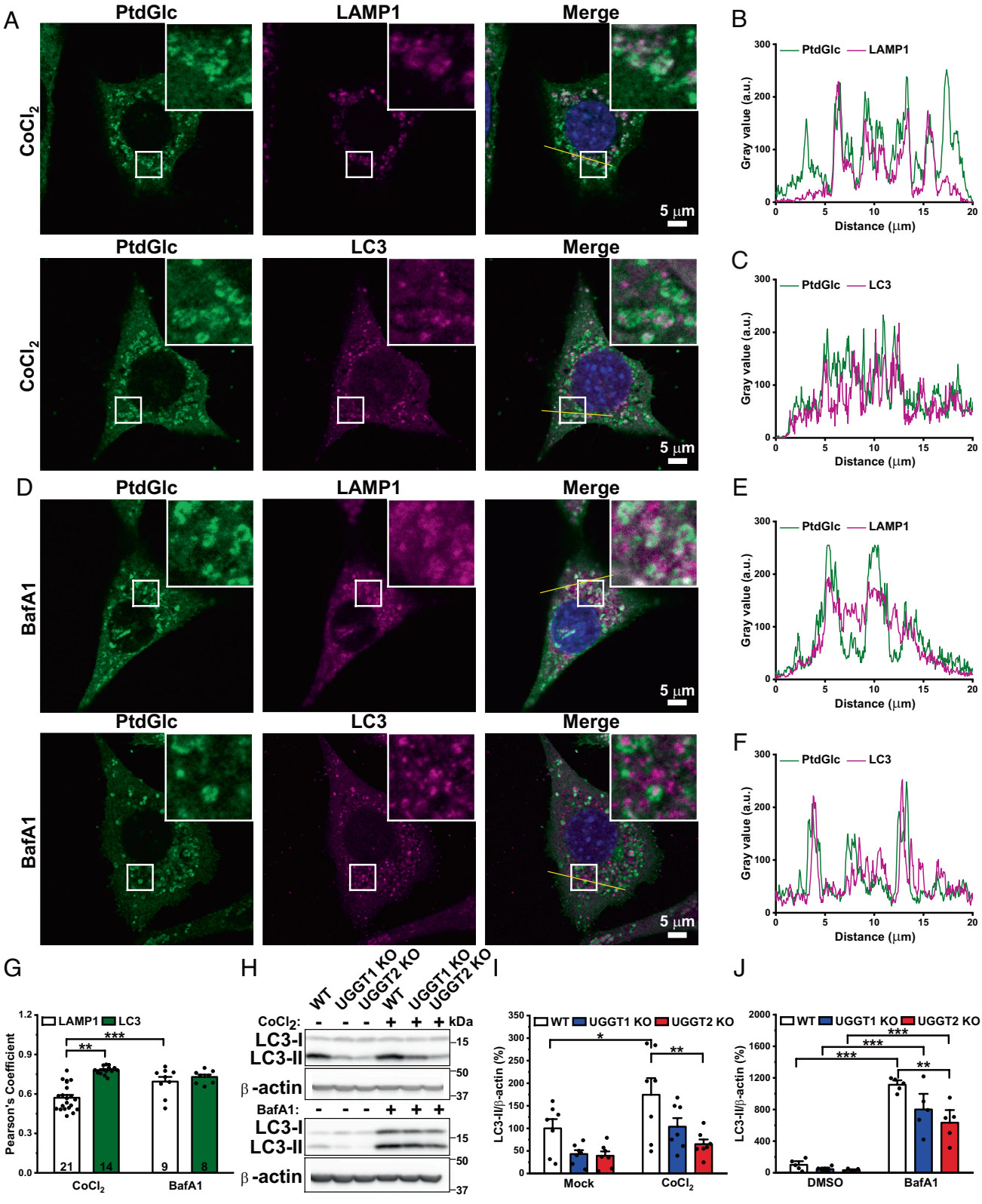

Fig. 4. Effects of UGGT2-dependent PtdGlc synthesis on autophagy under hypoxic conditions. (*A*) Representative confocal images showing punctate PtdGlc immunostaining (green) in WT MEFs treated with 200 μM $CoCl_2$ for 24 h. (*B*) Representative line profile plot showing the intensity distribution of green and magenta channels in the upper merged panel (yellow line) in (*A*). (*C*) Representative line profile plot showing the intensity distribution of green and magenta channels in the lower merged panel (yellow line) in (*A*). (*D*) Representative confocal images showing punctate PtdGlc immunostaining (green) in WT MEFs treated with 50 nM BafA1 for 25 h; BafA1 inhibits later stages of autophagy. (*E*) Representative line profile plot showing the intensity distribution of green and magenta channels in the upper merged panel (yellow line) in (*D*). (*F*) Representative line profile plot showing the intensity distribution of green and magenta channels in the lower merged panel (yellow line) in (*D*). In (*A*) and (*D*), the cells were also immunostained for the lysosomal network proteins LAMP1 (lysosomes) and LC3 (autophagosomes) (both magenta) and then stained with DAPI (blue). (*G*) Average Pearson's correlation coefficient assessing the extent of colocalization between green (PtdGlc) and magenta channels (LAMP1 or LC3). *N* values are indicated in the figure. (*H*) Representative western blots of LC3 from MEFs treated with $CoCl_2$ (200 μM, for 24 h) or BafA1 (50 nM, for 25 h). (*I*) Average normalized LC3-II levels ($N = 7$). (*J*) Average normalized LC3-II levels ($N = 5$). Data are means ± SEM and were analyzed by two-way ANOVA followed by Tukey's multiple comparison post hoc test; $^{*}P < 0.05$, $^{**}P < 0.01$, $^{***}P < 0.001$.

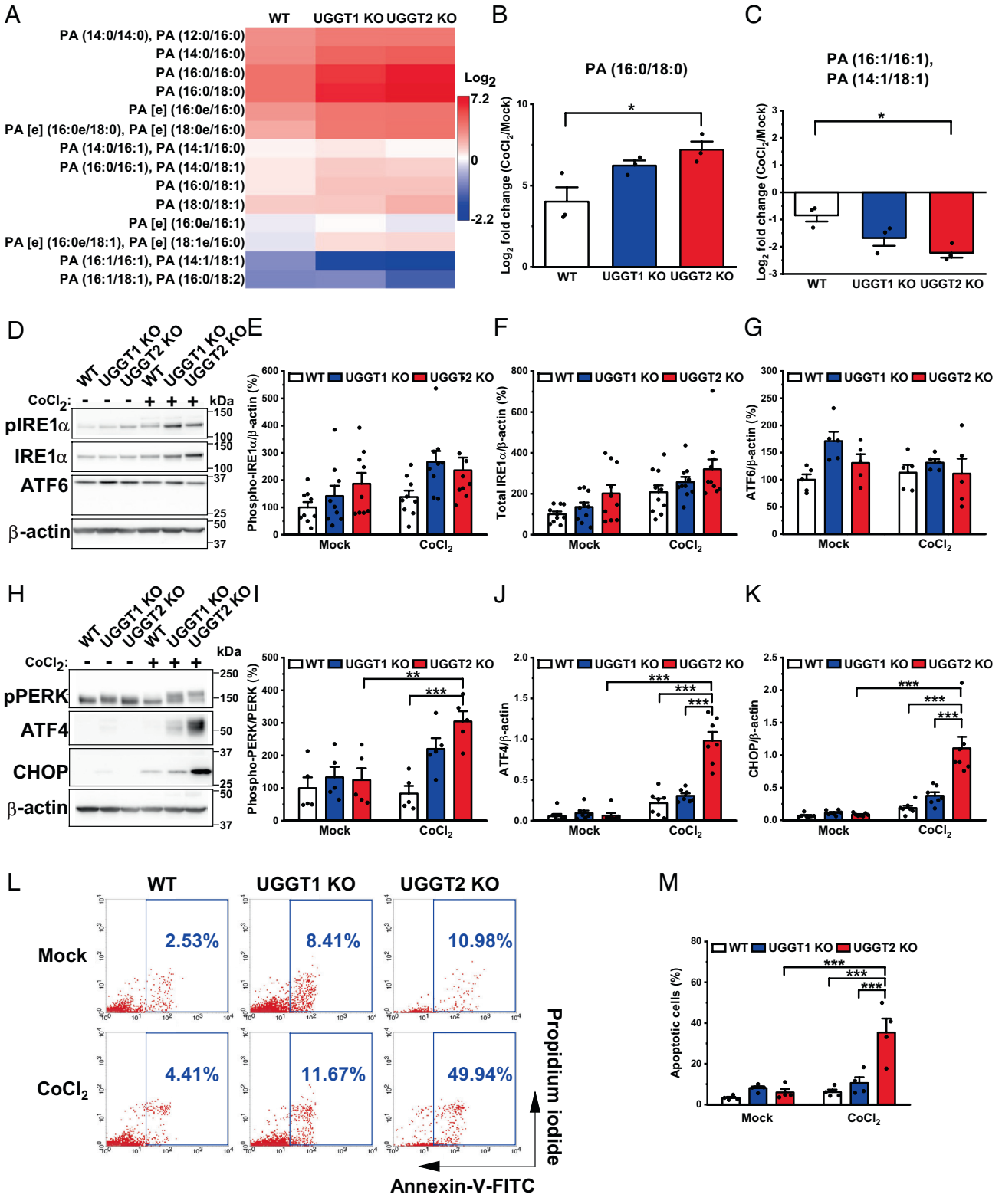

Fig. 5. Hypoxia-induced lipid bilayer stress activates PERK-CHOP-regulated apoptotic pathway in UGGT2-deficient cells. (*A*) Heatmap comparison of PA in WT, UGGT1 KO, and UGGT2 KO MEFs treated with $CoCl_2$ (200 μM, for 24 h). (*B*) Average $\log_2$ fold change in sPA (16:0/18:0) levels. (*C*) Average $\log_2$ fold change in uPAs (16:1/16:1, 14:1/18:1) levels. In (*B*) and (*C*), statistical differences were assessed by one-way ANOVA followed by Tukey's multiple comparison post hoc test ($N = 3$); $^*P < 0.05$. (*D*) Representative western blots of phosphor-IRE1α, IRE1α, and cleaved ATF6 from MEFs treated with $CoCl_2$ (200 μM, for 24 h). (*E*) Average normalized phospho-IRE1α levels ($N = 9$). (*F*) Average normalized IRE1α levels ($N = 10$). (*G*) Average normalized cleaved ATF6 levels ($N = 5$). (*H*) Representative western blots of phospho-PERK, ATF4, and CHOP from MEFs treated with $CoCl_2$ (200 μM, for 24 h). (*I*) Average normalized phospho-PERK levels ($N = 5$). (*J*) Average normalized ATF4 levels ($N = 7$). (*K*) Average normalized CHOP levels ($N = 7$). (*L*) Representative flow cytometric dot plots of apoptotic cells. (*M*) Average percentage of apoptotic cells from the parent gate ($N = 4$). Data are means ± SEM and were analyzed by two-way ANOVA followed by Tukey's multiple comparison post hoc test; $^*P < 0.05$, $^{**}P < 0.01$, $^{***}P < 0.001$.

UGGT1 is well established as a central component of the PQC system, tasked to maintain the balance between incompletely folded/misfolded proteins and correctly folded proteins. Re-glucosylation of incompletely folded/misfolded proteins by UGGT1 facilitates their re-entry into the protein folding cycle, enhancing the production rate of correctly folded proteins and the management of cellular energy usage. Terminally misfolded proteins evade re-glucosylation and are directed toward the degradation via ER-associated degradation (ERAD). This raises the question whether UGGT2 performs an analogous role in the ER quality control system but is focused on lipids. In this context, we propose that UGGT2 plays an important role in the ER by removing excess saturated lipids and alleviating lipid bilayer stress.

However, our findings do not negate the possible involvement of UGGT2 in protein re-glucosylation, especially upon *Uggt1* deletion. While *Uggt1* deletion in mice results in embryonic lethality, the viability of UGGT1 KO MEFs (20) indicates the presence of a complementary system potentially involving UGGT2. This is further corroborated by the increased expression of UGGT2 in UGGT1 KO MEFs (Fig. 3*D*), the demonstrated competition between sPA and urea-denatured Tg (Fig. 3*F*), and the reduced PtdGlc levels in WT MEFs upon misfolded protein stress (Fig. 3*G*). Taken together, this suggests that the presence of unfolded/misfolded proteins affects UGGT2-dependent lipid glucosylation and thus can rationalize the reduced PtdGlc levels observed in UGGT1 KO MEFs (Fig. 3 *A*–*C*). In HeLa cells, UGGT1 is expressed about 26 times more than UGGT2 (38). Our results also demonstrate that UGGT2 is dispensable for unfolded/misfolded protein glucosylation (*SI Appendix*, Fig. S1). Under basal conditions, UGGT1 alone is sufficient to ensure the optimal function of the protein folding machinery by re-glucosylating unfolded/misfolded proteins in WT MEFs, while UGGT2 is mainly responsible for lipid glucosylation.

Under normoxia, sFAs are efficiently converted to uFAs by ER-associated SCDs (39). The resulting uFAs are further processed into membrane lipids, such as phospholipids and sphingolipids, or stored as triglycerides in lipid droplets. Under hypoxic conditions, fatty acid biosynthesis increases via HIF-1α signaling (33), while progressively decreasing oxygen levels negatively affect SCD function (40) and increase the pool of sFAs. The resulting sFAs are gradually incorporated into saturated lipids such as sPA and ceramide (41). Under chemical hypoxia, a similar effect on the SCD-regulated fatty acid desaturation was observed. sPAs accumulated in MEFs under chemically induced hypoxic conditions (Fig. 5 *A* and *B*), while the levels of uPAs were decreased (Fig. 5 *A* and *C*).

Saturated lipids but not unsaturated lipids induce lipotoxicity in human vascular smooth muscle cells and inhibit the mammalian target of rapamycin complex 2 in mouse hepatocytes, resulting in insulin resistance (9, 42). In the presence of UGGT2, excess saturated lipids can be removed from the ER by, for example, glucosylation of toxic sPA and shuttling of the produced PtdGlc to the LE/Lys system, as evidenced by PtdGlc accumulation in the LE/Lys system (Fig. 4*A*). Under extended hypoxic conditions, or in the absence of UGGT2, the loss of ER membrane lipid quality is directly detected by the transmembrane domains of PERK (10), inducing CHOP-mediated apoptosis (Fig. 5 *K* and *L*). Reduced lipid quality is characterized by local abnormalities in membrane composition, fluidity, and packing density. The presence of a predicted hypoxia-inducible factor binding site on the promoter region of *Uggt2* further strengthens the role of UGGT2 in mitigating lipid bilayer stress under hypoxic conditions.

PtdGlc, a relatively recently discovered lipid, is only a trace constituent of the cellular phospholipidome under basal conditions. It is exclusively modified to contain sFA residues in rodent brain (24) and has been reported to preferentially form PtdGlc-rich membrane domains in biomembranes (43, 44). Because PtdGlc was localized to LE/Lys membrane, it is impossible to be directly degraded by lysosomal enzymes. It is tempting to speculate that PtdGlc-rich subdomains in lysosomal membrane initiate inward budding to form lysosomal intraluminal vesicles and are then available to be degraded by lysosomal enzymes (45). In addition, considering the ER-lysosome-autolysosome PtdGlc transport under lipid bilayer stress (Fig. 4 *A* and *D*), PtdGlc-rich subdomains in lysosomal membrane may act as platforms to recruit the autophagosome–lysosome fusion machinery. In addition, PtdGlc-rich subdomains in the ER membrane may be involved in the initial step of autophagosome formation considering reduced LC3 lipidation in UGGT2 KO MEFs (Fig. 4 *H*–*J*), though the detailed mechanisms will require further investigation in the future. Nevertheless, failure to induce autophagy in PtdGlc-deficient UGGT2 KO MEFs under stress leads to elevated PERK-ATF4-CHOP activation and apoptosis (Fig. 5 *H*–*M*).

How might our findings relate to disease pathophysiology? In general, hypoxia and dysregulation of cellular lipid saturation are associated with a variety of pathological conditions, including cancer and type II diabetes. Specifically, the response of cancer cells to hypoxia has been reported to be associated with therapy resistance (46). According to the Human Protein Atlas, UGGT2 expression levels and the survival rate of patients with lung or liver cancer exhibit an inverse correlation ($P < 0.001$) and thus is associated with an unfavorable prognosis (47). Our preliminary results demonstrate that loss of UGGT2 in mice increased susceptibility to HFD-induced obesity and concomitantly elevated fasting glucose levels (*SI Appendix*, Fig. S2), a hallmark of early onset type II diabetes. The analysis of human autopsy samples shows that CHOP expression is elevated only in pancreatic β-cells of patients with type II diabetes but not in patients with type I diabetes (48). The expression of UGGT2 was lower in β-cells of diabetic patients, and these β-cells were more susceptible to ER stress compared to β-cells from nondiabetic patients (16). Because the loss of UGGT2 in MEFs increased CHOP-regulated apoptosis under lipid-induced ER stress (Figs. 1 *A*–*D* and 5 *H*–*M*), reduced UGGT2 levels in diabetic β-cells can lead to CHOP-regulated apoptosis, and the subsequent loss of β-cells may contribute to the development of type II diabetes. Type II diabetes is known to be associated with abnormal lipid metabolism, supporting the hypothesis that UGGT2 plays an important role in maintaining lipid homeostasis and alleviating lipid bilayer-associated stress at least at a cellular level. In conclusion, we believe that the lipid bilayer-regulating capacity of UGGT2 described in the present work represents a novel pharmacological target.

Materials and Methods

Reagents and Antibodies. Monoclonal antibody DIM21, an anti-glycophospholipid PtdGlc antibody, was produced and purified as described previously (49). Synthetic PtdGlc was prepared according to a previous report (50). UGGT1 KO MEFs, UGGT2 KO MEFs, and sPA having sFAs (18:0/20:0) were prepared as described in the *SI Appendix*. The information on antibodies and reagents used in this study is also described in the *SI Appendix*.

Cell Culture and Drug Treatments. MEFs were maintained in Dulbecco's modified Eagle's medium (DMEM) supplemented with 10% fetal bovine serum (FBS), 1 mM sodium pyruvate, and nonessential amino acids solution (NEAA). Chinese hamster ovary (CHO) cells were maintained in DMEM supplemented with 10% FBS, L-glutamine, and 1% penicillin/streptomycin. All cells were cultured at 37 °C in a 5% CO_2-humidified atmosphere. For CAY10566, tunicamycin, DTT, or $CoCl_2$ treatments, MEFs were cultured in FBS-free DMEM supplemented with 1 mM

sodium pyruvate and NEAA and then treated with 5 μM CAY10566 at 37 °C for 24 h, with 1 μM tunicamycin at 37 °C for 24 h, with 10 μM tunicamycin at 37 °C for 6 h, with 10 mM DTT at 37 °C for 6 h, with 50 nM BafA1 at 37°C for 25 h, or with 200 μM $CoCl_2$ at 37 °C for 24 h.

Immunofluorescent Labeling of Cultured Cells and Imaging. Cultured cells grown on coverslips or cells collected from the cultures were fixed for 20 min with 4% paraformaldehyde diluted with Dulbecco's phosphate buffered saline (PBS, 137 mM NaCl, 2.7 mM KCl, 8.1 mM Na_2HPO_4, 1.5 mM KH_2PO_4), and then washed three times with PBS. Nonspecific binding was blocked with 4% normal goat serum, and then the cells were permeabilized for 15 min with 0.1% Triton X-100 in PBS. Permeabilized cells were washed three times with PBS, immunostained with a monoclonal anti-PtdGlc antibody (DIM21) at 4 °C overnight. After washing out excess primary antibody, cells were incubated at room temperature for 1 h with secondary antibody (Alexa Fluor 488 anti-mouse IgM or Alexa Fluor 568 anti-mouse IgM). Labeled cells were prepared for imaging by coverslipping with Shandon Immu-mount or Fluoromount-G Mounting Medium (with DAPI). Fluorescence was observed and documented with a confocal microscope (Leica TCS SP8). Alternatively, the cells collected from cultures were analyzed by flow cytometry using a BD Biosciences LSR II instrument. To examine the intracellular localization of PtdGlc, cells were co-immunostained with an anti-LAMP1 antibody or an anti-LC3 antibody.

Protein Purification. CHO cells were transfected with flag-tagged *Uggt1* or *Uggt2* plasmids using Lipofectamine LTX reagent according to the manufacturer's instructions. After 24 h, cells were collected and suspended in Tris buffer solution (TBS, 25 mM NaCl, 137 mM NaCl, and 3 mM KCl) containing proteinase inhibitor. Cells were lysed using an ultrasonicator (Vibra-Cell GE 130PB, Newtown, CT, USA) and centrifuged at 800 × *g* for 5 min. The supernatant was collected and centrifuged for 1 h at 100,000 × *g* (Beckman Coulter Optima MAX-TL). The pellet was lysed at 4 °C for 1 h in 1% Igepal in TBS containing proteinase inhibitor, followed by centrifugation at 800 × *g* for 5 min. The supernatant, microsome lysate, was collected and incubated with anti-flag M2 affinity gel at 4 °C overnight. After washing the gel with TBS three times, UGGT1 or UGGT2 proteins were competitively eluted with 200 μg/mL 3× flag peptide solution. Samples containing UGGT1 or UGGT2 proteins were passed through the Amicon® Ultra-0.5 Centrifugal Filter Devices (MilliporeSigma) following the manufacturer's instructions to remove 3× flag peptide and to be concentrated.

The concentration and purity of samples were examined by the CBB staining. One-twentieth of the samples was denatured at 95 °C for 10 min, separated on an Extra PAGE One Precast Gel (5 to 20% or 15%), and then gel was stained by CBB Stain One according to the manufacturer's instructions.

In Vitro Enzymatic Assay of PtdGlc Synthesis. The synthetic saturated PA (18:0/20:0) or uPA (18:1/18:1) was dissolved in 1% Igepal or 1% Triton X-100, incubated with purified flag-UGGT1 or flag-UGGT2 protein at 40 °C for 1 h, and then incubated at 37 °C overnight. The assay solution contained 10 mM Tris-HCl (pH 8.1), 200 μM UDP-glucose, 1 mM $CaCl_2$, and 1 mM $MgCl_2$. The reaction was stopped by adding 1:2 (v/v) chloroform–methanol mixture, and the lipids were extracted according to a modified Bligh and Dyer procedure (51). The extracted lipids were thoroughly dried under N_2 gas.

The extracted lipids from the in vitro enzymatic assay were analyzed on a triple quadrupole liquid chromatograph mass spectrometer (Shimadzu Corporation LCMS-8060). The dried lipids were dissolved in methanol and loaded into a Mastro2 C18 column (2.0 mm × 100 mm, particle size: 2.2 μM, Shimadzu Corporation) maintained at 80 °C. Solvent A was 50% acetonitrile/50% 5 mM ammonium formate and solvent B was 10:90 (v/v) acetonitrile–isopropanol mixture. The lipids were eluted with a linear gradient of solvent B (from 40 to 98% within 50 min, holding 20 min) and at a flow rate of 0.1 mL/min. The electrospray ionization source was operated in negative ion mode, and PtdGlc (18:0/20:0) was detected with multiple reaction monitoring utilizing four precursor–product ion pairs simultaneously at the following settings: *m/z* 893.5 → 283.1 (CE: 66.0); *m/z* 893.5 → 311.2 (CE: 56.0); *m/z* 893.5 → 419.1 (CE: 37.0); and *m/z* 893.5 → 79.0 (CE: 97.0). The glucosylated-uPA (18:1/18:1) was detected with multiple reaction monitoring utilizing three precursor–product ion pairs simultaneously at the following settings: *m/z* 861.5 → 281.1 (CE: 66.0); *m/z* 861.5 → 417.1 (CE: 37.0); and *m/z* 861.5 → 79.0 (CE: 97.0).

For thyroglobulin inhibition experiments, the assay solution also contained 8 M urea-denatured thyroglobulin. Thyroglobulin was incubated with 8 M urea at 32 °C for 48 h, and then a diafiltration step was performed by using the Amicon® Ultra-0.5 Centrifugal Filter Devices (MilliporeSigma) following the manufacturer's instructions to remove urea.

Unbiased Lipidomics Methods. Unbiased lipidomics was performed as described previously (52). Briefly, the dried cell fraction was re-dissolved in 200 μL of methanol containing EquiSPLASH (for internal standards). After sonication for 30 s, 150 μL of the cell suspension was transferred to a glass tube, 75 μL of chloroform was added, and the mixture was vigorously agitated at 20 °C for 20 min. Subsequently, 15 μL of water was added, and the mixture was vigorously agitated at 20 °C for 20 min. The mixture underwent centrifugation at 1,670 x *g* at 20 °C for 10 min, and then the supernatant was collected and transferred to a liquid chromatography (LC) vial.

To determine the levels of unsaturated- and saturated lipids under hypoxic condition, we performed LC-mass spectrometry analysis using a quadruple time-of-flight instrument (Q TOF)/MS (SCIEX TripleTOF 6600) coupled with an ACQUITY UPLC system (Waters Corporation); analysis was described in detail previously (53, 54). LC separation was performed with a gradient elution of mobile phase A (methanol/acetonitrile/water (1:1:3, v/v/v) containing 5 mM ammonium acetate and 10 nM EDTA) and mobile phase B (isopropanol containing 5 mM ammonium acetate and 10 nM EDTA). The flow rate was 300 μL/min at 45 °C using a L-column3 C18 (50 × 2.0 mm i.d., particle size 2.0 μM, Chemicals Evaluation and Research Institute). The injection volume was 3 μL in negative-ion mode and positive-ion mode. Raw data files from the Q TOF/MS were converted to Mascot Generic Format (proprietary SCIEX format) files using the SCIEX MS converter for the quantitative analysis with 2DICAL (Mitsui Knowledge Industry Co., Ltd.). Identification of the molecular species was accomplished by comparing retention times and MS/MS spectra data from the information-dependent acquisition mode.

Cell Viability Assay. Cells were cultured in 24-well plates at a density of 5 × 10^5 cells per well. After treatment with DTT (10 mM) for 6 h, cells were washed three times with PBS and incubated with culture medium containing 0.4 mg/mL 3-(4,5-dimethylthiazol-2-yl)-2,5-diphenyltetrazolium bromide (MTT) at 37 °C for 4 h. The MTT solution was then carefully aspirated off, and 0.5 mL of DMSO was added into each well to dissolve the purple formazan crystals. Quantitative measurements were made with a multi-well spectrophotometer (Model 680 Microplate Reader, Hercules) at an absorbance of 570 nm.

To assess the role of UGGT2 in alleviating hypoxia-associated lipid bilayer stress, we measured lipid saturation with $CoCl_2$, a hypoxia-mimetic agent. Cultured cells were treated with $CoCl_2$ (200 μM) for 24 h and then washed three times with PBS. Cells were collected and incubated with Annexin V-FITC and propidium iodide (PI) following the manufacturer's instructions. Apoptotic cells were then analyzed by flow cytometry (BD Biosciences LSR II).

Western Blot Analysis. Cultured cells were washed with PBS three times and then suspended in 1% Igepal dissolved in a solution of ice-cold TBS containing proteinase inhibitor and phosphatase inhibitor. Cells were lysed briefly using an ultrasonicator (Vibra-Cell™ GE 130PB) and then put on ice for 15 min. The lysates were centrifuged at 14,000 × *g* for 15 min, and the supernatants were collected for the western blot assay. Protein concentration was determined by bicinchoninic acid protein assay (55). The protein mixture was denatured at 95 °C for 10 min, separated on an Extra PAGE One Precast Gel (5 to 20% or 15%), and then separated proteins were transferred onto nitrocellulose membranes. Membranes were incubated with primary antibody at 4 °C overnight, followed by horseradish peroxidase-conjugated secondary antibody at room temperature for 1 h. Immunoreactive bands were visualized with ImmunoStar Zeta or Long Detection reagents according to the manufacturer's instructions, and the signals were detected on an ImageQuant LAS 4000 (Cytiva). The blot densitometry was quantitated by ImageJ software (NIH)

Data Analysis. All statistical analyses were done with GraphPad Software Prism. Data are presented as means ± SEM. Significant differences were evaluated with, where appropriate, Student's *t* test, paired *t* test, one-way ANOVA followed by Tukey's multiple comparison post hoc test or Dunnett's multiple comparison post hoc test, or two-way ANOVA followed by Tukey's multiple comparison post hoc test or Sidak multiple comparison post hoc test. Differences were considered

statistically significant at $P < 0.05$. All images were analyzed by ImageJ software (NIH). All graphs were created by Origin 2020 (OriginLab).

Data, Materials, and Software Availability. The data supporting the findings of this study are available within the *SI Appendix*. The LC-MS/MS data have been deposited in Figshare at 10.6084/m9.figshare.21316299.

ACKNOWLEDGMENTS. We thank Ms. Fujinawa's help with animal care. We thank Mr. Yuuya Senoo and Mrs. Rumi Ikeda for their cooperation in MS analysis. This work was supported in part by Japan Agency for Medical Research and Development (AMED-CREST) Grant Number 20gm0910006h0005 (H.K.); Japan Society for the Promotion of Science (JSPS) Grants-in-Aid for Scientific Research (KAKENHI) Grant Numbers 16K08259 (P.G.) and 16H06290 (Y.H.); Mizutani Foundation for Glycoscience (P.G. and Y.H.); and Glycolipidologue Program of RIKEN (P.G., Y.H., and H.K.). M.M. was supported by Signora Alessandra, AlphaONE Foundation, Foundation for Research on Neurodegenerative Diseases, Swiss NSF (SNSF), and Comel and Gelu Foundations. R.J.K. was partially supported by NIH (NIH) Grant numbers CA198103, DK103185, DK113171, and AG062190.

Author affiliations: [a]RIKEN Center for Brain Science, Wako, Saitama 351-0198, Japan; [b]Faculty of Biomedical Sciences, Institute for Research in Biomedicine, Università della Svizzera Italiana, 6500 Bellinzona, Switzerland; [c]Degenerative Diseases Program, Sanford Burnham Prebys Medical Discovery Institute, La Jolla, CA 92037; [d]Institute for Environmental and Gender-Specific Medicine, Juntendo University Graduate School of Medicine, Chiba 279-0021, Japan; [e]Division of Molecular Science, Gunma University, Maebashi 371-8510, Japan; [f]Laboratory of Biomolecule Analysis, Kazusa DNA Research Institute, Chiba 292-0818, Japan; [g]School of Life Sciences, École Polytechnique Fédérale de Lausanne, 1015 Lausanne, Switzerland; and [h]RIKEN Cluster for Pioneering Research, RIKEN, Wako, Saitama 351-0198, Japan

1. C. K. Barlowe, E. A. Miller, Secretory protein biogenesis and traffic in the early secretory pathway. *Genetics* **193**, 383–410 (2013).
2. P. Fagone, S. Jackowski, Membrane phospholipid synthesis and endoplasmic reticulum function. *J. Lipid. Res.* **50**, S311–S316 (2009).
3. J. H. Lin, P. Walter, T. S. Yen, Endoplasmic reticulum stress in disease pathogenesis. *Annu. Rev. Pathol.* **3**, 399–425 (2008).
4. K. Araki, K. Nagata, Protein folding and quality control in the ER. *Cold. Spring Harb. Perspect. Biol.* **4**, a015438 (2012).
5. C. Hammond, I. Braakman, A. Helenius, Role of N-linked oligosaccharide recognition, glucose trimming, and calnexin in glycoprotein folding and quality control. *Proc. Natl. Acad. Sci. U.S.A.* **91**, 913–917 (1994).
6. C. Labriola, J. J. Cazzulo, A. J. Parodi, Retention of glucose units added by the UDP-GLC:glycoprotein glucosyltransferase delays exit of glycoproteins from the endoplasmic reticulum. *J. Cell Biol.* **130**, 771–779 (1995).
7. D. A. Cunha *et al.*, Initiation and execution of lipotoxic ER stress in pancreatic beta-cells. *J. Cell Sci.* **121**, 2308–2318 (2008).
8. S. Fu *et al.*, Aberrant lipid metabolism disrupts calcium homeostasis causing liver endoplasmic reticulum stress in obesity. *Nature* **473**, 528–531 (2011).
9. M. Masuda *et al.*, Saturated phosphatidic acids mediate saturated fatty acid-induced vascular calcification and lipotoxicity. *J. Clin. Invest.* **125**, 4544–4558 (2015).
10. R. Volmer, K. van der Ploeg, D. Ron, Membrane lipid saturation activates endoplasmic reticulum unfolded protein response transducers through their transmembrane domains. *Proc. Natl. Acad. Sci. U.S.A.* **110**, 4628–4633 (2013).
11. D. A. Caraballo *et al.*, Origin and evolution of two independently duplicated genes encoding UDP-glucose: Glycoprotein glucosyltransferases in caenorhabditis and vertebrates. *G3 (Bethesda)* **10**, 755–768 (2020).
12. S. M. Arnold, L. I. Fessler, J. H. Fessler, R. J. Kaufman, Two homologues encoding human UDP-glucose:glycoprotein glucosyltransferase differ in mRNA expression and enzymatic activity. *Biochemistry* **39**, 2149–2163 (2000).
13. B. M. Adams, N. P. Canniff, K. P. Guay, I. S. B. Larsen, D. N. Hebert, Quantitative glycoproteomics reveals cellular substrate selectivity of the ER protein quality control sensors UGGT1 and UGGT2. *Elife* **9**, e63997 (2020).
14. P. Kim, M. R. Scott, J. H. Meador-Woodruff, Abnormal expression of ER quality control and ER associated degradation proteins in the dorsolateral prefrontal cortex in schizophrenia. *Schizophr. Res.* **197**, 484–491 (2018).
15. A. Y. Taha, Y. Cheon, K. Ma, S. I. Rapoport, J. S. Rao, Altered fatty acid concentrations in prefrontal cortex of schizophrenic patients. *J. Psychiatr. Res.* **47**, 636–643 (2013).
16. P. Marchetti *et al.*, The endoplasmic reticulum in pancreatic beta cells of type 2 diabetes patients. *Diabetologia* **50**, 2486–2494 (2007).
17. S. M. Arnold, R. J. Kaufman, The noncatalytic portion of human UDP-glucose: Glycoprotein glucosyltransferase I confers UDP-glucose binding and transferase function to the catalytic domain. *J. Biol. Chem.* **278**, 43320–43328 (2003).
18. Y. Takeda *et al.*, Both isoforms of human UDP-glucose:glycoprotein glucosyltransferase are enzymatically active. *Glycobiology* **24**, 344–350 (2014).
19. M. Miyazaki, J. M. Ntambi, Role of stearoyl-coenzyme A desaturase in lipid metabolism. *Prostaglandins Leukot. Essent. Fatty Acids* **68**, 113–121 (2003).
20. K. J. Mitchell *et al.*, Functional analysis of secreted and transmembrane proteins critical to mouse development. *Nat. Genet.* **28**, 241–249 (2001).
21. Y. Ishibashi, A. Kohyama-Koganeya, Y. Hirabayashi, New insights on glucosylated lipids: Metabolism and functions. *Biochim. Biophys. Acta* **1831**, 1475–1485 (2013).
22. S. Ichikawa, H. Sakiyama, G. Suzuki, K. I. Hidari, Y. Hirabayashi, Expression cloning of a cDNA for human ceramide glucosyltransferase that catalyzes the glycosylation step of glycosphingolipid synthesis. *Proc. Natl. Acad. Sci. U.S.A.* **93**, 4638–4643 (1996).
23. A. R. Marques *et al.*, Glucosylated cholesterol in mammalian cells and tissues: Formation and degradation by multiple cellular β-glucosidases. *J. Lipid. Res.* **57**, 451–463 (2016).
24. Y. Nagatsuka *et al.*, Phosphatidylglucoside exists as a single molecular species with saturated fatty acyl chains in developing astroglial membranes. *Biochemistry* **45**, 8742–8750 (2006).
25. S. E. Trombetta, M. Bosch, A. J. Parodi, Glucosylation of glycoproteins by mammalian, plant, fungal, and trypanosomatid protozoa microsomal membranes. *Biochemistry* **28**, 8108–8116 (1989).
26. E. Bobrovnikova-Marjon *et al.*, PERK utilizes intrinsic lipid kinase activity to generate phosphatidic acid, mediate Akt activation, and promote adipocyte differentiation. *Mol. Cell Biol.* **32**, 2268–2278 (2012).
27. T. Promlek *et al.*, Membrane aberrancy and unfolded proteins activate the endoplasmic reticulum stress sensor Ire1 in different ways. *Mol. Biol. Cell* **22**, 3520–3532 (2011).
28. T. Radanović, R. Ernst, The unfolded protein response as a guardian of the secretory pathway. *Cells* **10**, 2965 (2021).
29. A. Sundaram, S. Appathurai, R. Plumb, M. Mariappan, Dynamic changes in complexes of IRE1α, PERK, and ATF6α during endoplasmic reticulum stress. *Mol. Biol. Cell* **29**, 1376–1388 (2018).
30. K. Halbleib *et al.*, Activation of the unfolded protein response by lipid bilayer stress. *Mol. Cell* **67**, 673–684.e678 (2017).
31. D. Ackerman, M. C. Simon, Hypoxia, lipids, and cancer: Surviving the harsh tumor microenvironment. *Trends Cell Biol.* **24**, 472–478 (2014).
32. R. M. Young *et al.*, Dysregulated mTORC1 renders cells critically dependent on desaturated lipids for survival under tumor-like stress. *Genes Dev.* **27**, 1115–1131 (2013).
33. E. Furuta *et al.*, Fatty acid synthase gene is up-regulated by hypoxia via activation of Akt and sterol regulatory element binding protein-1. *Cancer Res.* **68**, 1003–1011 (2008).
34. S. Wilkinson, ER-phagy: Shaping up and destressing the endoplasmic reticulum. *FEBS J.* **286**, 2645–2663 (2019).
35. M. Loi, A. Raimondi, D. Morone, M. Molinari, ESCRT-III-driven piecemeal micro-ER-phagy remodels the ER during recovery from ER stress. *Nat. Commun.* **10**, 5058 (2019).
36. I. Fregno *et al.*, ER-to-lysosome-associated degradation of proteasome-resistant ATZ polymers occurs via receptor-mediated vesicular transport. *EMBO J.* **37**, e99259 (2018).
37. Y. Ichimura *et al.*, A ubiquitin-like system mediates protein lipidation. *Nature* **408**, 488–492 (2000).
38. D. N. Itzhak, S. Tyanova, J. Cox, G. H. Borner, Global, quantitative and dynamic mapping of protein subcellular localization. *Elife* **5**, e16950 (2016).
39. L. Ellgaard, N. McCaul, A. Chatsisvili, I. Braakman, Co- and post-translational protein folding in the ER. *Traffic* **17**, 615–638 (2016).
40. J. J. Kamphorst *et al.*, Hypoxic and Ras-transformed cells support growth by scavenging unsaturated fatty acids from lysophospholipids. *Proc. Natl. Acad. Sci. U.S.A.* **110**, 8882–8887 (2013).
41. J. Korbecki, K. Bajdak-Rusinek, The effect of palmitic acid on inflammatory response in macrophages: An overview of molecular mechanisms. *Inflamm. Res.* **68**, 915–932 (2019).
42. D. Ryu *et al.*, TORC2 regulates hepatic insulin signaling via a mammalian phosphatidic acid phosphatase, LIPIN1. *Cell Metab.* **9**, 240–251 (2009).
43. M. Murate *et al.*, Phosphatidylglucoside forms specific lipid domains on the outer leaflet of the plasma membrane. *Biochemistry* **49**, 4732–4739 (2010).
44. H. Takahashi *et al.*, Phosphatidylglucoside: Its structure, thermal behavior, and domain formation in plasma membranes. *Chem. Phys. Lipids* **165**, 197–206 (2012).
45. S. Rudnik, M. Damme, The lysosomal membrane-export of metabolites and beyond. *FEBS J.* **288**, 4168–4182 (2021).
46. S. Chipurupalli, E. Kannan, V. Tergaonkar, R. D'Andrea, N. Robinson, Hypoxia induced ER stress response as an adaptive mechanism in cancer. *Int. J. Mol. Sci.* **20**, 749 (2019).
47. K. El Bairi, M. Amrani, S. Afqir, The human cancer pathology atlas: An open-access source for more than 900,000 Kaplan-Meier plots and 5 million cancer tissue images. *Biomed. Pharmacother.* **96**, 1438–1439 (2017).
48. C. J. Huang *et al.*, High expression rates of human islet amyloid polypeptide induce endoplasmic reticulum stress mediated beta-cell apoptosis, a characteristic of humans with type 2 but not type 1 diabetes. *Diabetes* **56**, 2016–2027 (2007).
49. Y. Yamazaki *et al.*, Comprehensive analysis of monoclonal antibodies against detergent-insoluble membrane/lipid rafts of HL60 cells. *J. Immunol. Methods* **311**, 106–116 (2006).
50. P. Greimel, Y. Ito, First synthesis of natural phosphatidyl-β-d-glucoside. *Tetrahedron Lett.* **49**, 3562–3566 (2008).
51. E. G. Bligh, W. J. Dyer, A rapid method of total lipid extraction and purification. *Can. J. Biochem. Physiol.* **37**, 911–917 (1959).
52. H. Tsugawa *et al.*, Comprehensive identification of sphingolipid species by in silico retention time and tandem mass spectral library. *J. Cheminform.* **9**, 19 (2017).
53. T. Hirabayashi *et al.*, PNPLA1 has a crucial role in skin barrier function by directing acylceramide biosynthesis. *Nat. Commun.* **8**, 14609 (2017).
54. H. Tsugawa *et al.*, A lipidome atlas in MS-DIAL 4. *Nat Biotechnol* **38**, 1159–1163 (2020).
55. J. M. Walker, The bicinchoninic acid (BCA) assay for protein quantitation. *Methods Mol. Biol.* **32**, 5–8 (1994).